Facile Preparation of Ultralong Dendritic PtIrTe Nanotubes and Their High Electrocatalytic Activity on Methanol Oxidation

Yanfei Hao,[†] Yunyun Yang,[†] Liji Hong,[†] Junhua Yuan,*[,†,‡] Li Niu,[§] and Yanghai Gui[∥]

[†]Key Laboratory of the Ministry of Education for Advanced Catalysis Materials, College of Life Sciences and Chemistry, Zhejiang Normal University, Jinhua, Zhejiang 321004, China

[‡]School of Pharmacy, Hubei University of Science and Technology, Xianning, Hubei 437100, China

[§]State Key Laboratory of Electroanalytical Chemistry, Changchun Institute of Applied Chemistry, The Chinese Academy of Sciences, Changchun, Jilin 130022, China

[∥]Henan Provincial Key Laboratory of Surface & Interface Science, Zhengzhou University of Light Industry, Zhengzhou, Henan 450002, China

S Supporting Information

ABSTRACT: A facile wet chemical approach was developed to prepare ultralong PtIrTe nanotubes (NTs) using Te nanowires (NWs) as template. These PtIrTe NTs were made up of Pt nanodendrites uniformly arrayed on the surface of IrTe NTs and interweaved with each other to nanopores. Their morphology, structure, and composition were investigated by transition electron microscopy, X-ray powder diffraction, and X-ray photoelectron spectroscopy. As expected, these PtIrTe NTs catalysts show a larger surface area, a stronger CO tolerance, and a higher catalytic activity toward electrochemical oxidation of methanol relative to the commercial Pt catalysts due to the 1D porous core−shell structure and the modification of the electronic effect by Ir.

KEYWORDS: core−shell, nanotube, methanol oxidation, electrocatalysis
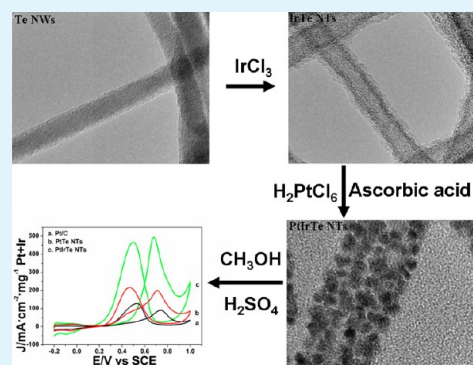
1. INTRODUCTION

Platinum (Pt) is an indispensible ingredient for numerous catalysts in industrial production and commercial devices because of its unique and versatile competence in the acceleration on the redox reactions of small molecules, such as methanol, alcohol, formic acid, et al.[1] A case in point is Pt catalysts widely used to convert methanol into CO_2 in the methanol fuel cells (DMFCs). As we all know, DMFCs hold the promise to be a potential energy for vehicles and portable devices on account of its great specific output density, high energy conversion efficiency, low starting temperature, and near-zero pollution emission.[2] In DMFCs, methanol oxidation is sluggish at the Pt crystal face. It involves a multielectron transfer. Moreover, Pt is prone to be poisoned by the intermediate species, such as CO. These byproducts will occupy the active sites of the Pt crystal plane by adsorption and block the transportation of methanol in its oxidation.[3] On the other hand, the wide application of Pt catalysts will result in the unbearable price for the commercial utility of DMFCs.

The cost-effective use of Pt catalysts should be borne in mind during the fabrication of the DMFCs, and toward this goal, an essential step is to engineer the structure and component of Pt catalysts with an aim to optimize their activity on methanol oxidation.[1−4] Morphology design is a popular approach. Recent attention focuses on the porous Pt nanostructures owing to their large specific surface areas and high-index exposed facets.[5] In parallel, increasing efforts have been poured into the preparation of multicomponent Pt catalysts in the shape of alloy, core−shell, and heterostructure.[6] Since only the Pt skin atoms in a catalyst are used in practice to boost a redox reaction while the Pt bulk atoms are needless, a multielement Pt catalyst is more economic for the usage of Pt in catalysts and less limited due to the reserve and economic dependence.[1] Moreover, a multielement Pt catalyst will be superior to its monometallic components due to a possible synergistic effect among Pt and non-Pt elements.[7,8]

In addition, one-dimensional (1D) Pt nanostructures have also obtained considerable interest in the field of catalysis.[9] The 1D Pt-based electrocatalysts have been prepared by colloid approach,[10,11] electrodeposition method,[12,13] and template strategy.[14−16] Xiao and co-workers have reported the one-pot method by polyols thermal reduction to synthesize ultrathin and ultralong single-crystal platinum nanowires (Pt NWs) assemblies.[10] Yuan and co-workers have proposed a one-step strategy by electrodeposition to prepare ordered Pt nanotube arrays in the porous anodic aluminum film.[13] Besides, 1D Pt
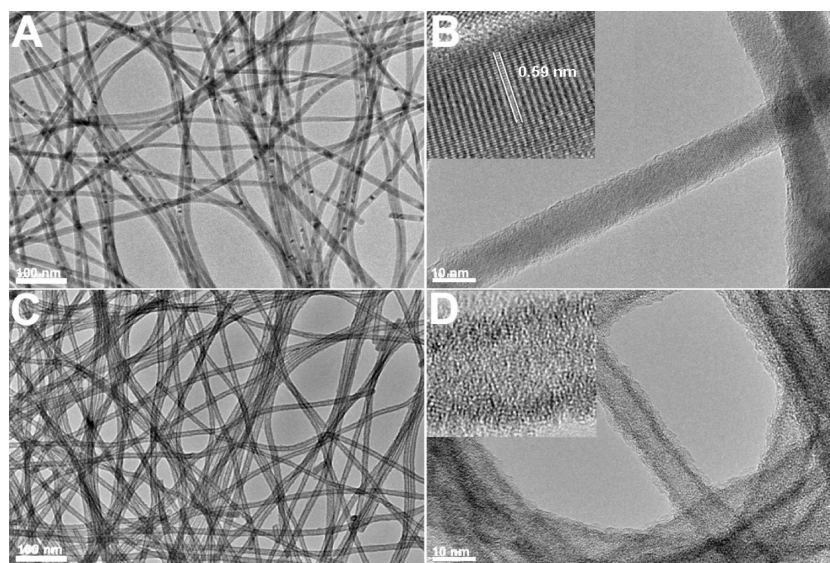
Figure 1. TEM images of Te NWs (A, B) and IrTe NTs (C, D) under different magnification (A, C) 100 nm, (B, D) 10 nm. Inset: their high resolution TEM images.

catalysts can be obtained by replacement reaction using Ag,[14] Cu,[17] Se,[18] or Te nanowires[15] as sacrificial templates.

Despite extensive investigation of these 1D Pt catalysts to date, the mass production of Pt NWs with a porous skin is far from meaningless with a view to the promise as high active and cost-effective catalysts used in the DMFCs.[1] Herein, we demonstrate a facile, solution approach to mass synthesis of ultralong PtIrTe tricomponent nanotubes (NTs) with the core made of IrTe NTs and the shells comprised of Pt nanodendrites. Interestingly, Pt nanodendrites are arrayed on IrTe NTs and interweaved with each other to form a porous structure among IrTe NTs. As expected, these ultralong nanodendritic Pt on IrTe NTs exhibit a high surface area, which will enhance electrocatalytic activity toward methanol oxidation reaction (MOR).

2. EXPERIMENTAL SECTION

2.1. Chemicals and Materials. Polyvinylpyrrolidone (PVP, Mw ca. 58000) was purchased from Acros. Na_2TeO_3, H_2PtCl_6, $IrCl_3$, H_2SO_4 (98%), and methanol were purchased from Shanghai reagent Co. Inc. Pt/C (25%) was purchased from De Nora Elettrodi Co. Ltd. Water was purified and deionized by a Milli-Q system.

2.2. Preparation of Te NWs. Te NWs were prepared by a slight modification of the method according to ref 15. 0.20 mg of PVP was dissolved into 20 mL of the deionized water in an ultrasonic bath. Then, 111 mg of Na_2TeO_3 was dissolved into the solution, followed by introducing hydrazine hydrate (85%, 1 mL) and ammonia solution (25−28%, 2 mL). This mixture was sealed in a Teflon-lined stainless steel autoclave and maintained at 180 °C for 8 h, and, last, the samples were allowed to cool down. The Te NWs were precipitated with acetone, recovered after centrifugation, and washed with water and ethanol. These Te NWs (50 mg) were redispersed into the solution (100 mL) containing glycol and ethanol with a volume ratio of 1:1 by an ultrasonic method for further preparation of IrTe NTs, PtTe NTs, and PtIrTe NTs.

2.3. Preparation of PtTe NTs and IrTe NTs. PtTe NTs were synthesized via a replacement reaction in line with ref 5. 200 μL of 0.5 M H_2PtCl_6 was added into 20 mL of Te NWs dispersion, and then Te NWs reacted with H_2PtCl_6 at 50 °C for 12 h under magnetic stirring. PtTe NTs were recovered by centrifugation and washed with water and ethanol.

The preparation of IrTe NTs is similar to the synthetic procedures for the PtTe NTs via the replacement of Te by Ir at 90 °C for 12 h.

2.4. Preparation of PtIrTe NTs. The PtIrTe NTs were prepared by in situ precipitation of Pt nanoparticles on IrTe NTs using ascorbic acid (AA) as reductant. 50 mg of PVP and 100 mg of AA were dissolved into 20 mL of the deionized water. 10 mg of IrTe NTs was added and dispersed into the mixture solution under ultrasonic agitation. The IrTe NTs dispersion was saturated with N_2 and transferred into a flask after addition of 200 μL of H_2PtCl_6 (0.5 M). The Pt precursors were reduced by AA and deposited on IrTe NTs after magnetic stirring at 90 °C for 2 h.

2.5. Composition and Structure Analysis. X-ray photoelectron spectroscopy (XPS), thermogravimetric analysis (TGA), and the inductively coupled plasma-atom emission spectroscopy (ICP-AES) were used to examine the composition of the as-prepared products. XPS were conducted on an ESCALAB-MKII spectrometer with an unmonochromated Al KR X-ray source (1486.6 eV) for excitation. TGA data were collected on a Netzsch STA 449C analyzer at a heating rate of 10 °C/min under nitrogen. The ICP-AES technique was carried out on a PerkinElmer ICP-Optima 4300. The samples were dissolved into 3:1 concentrated HCl:HNO$_3$ and diluted to an appropriate volume before being induced to the plasma. Intensities are measured at Te 214.281 nm, Pt 340.458 nm, and Ir 205.222 nm.

Transmission electron microscopy (TEM) and X-ray diffraction (XRD) analyses were used to observe nanoscale structure and determine crystalline phase of the as-prepared products. TEM images were obtained from a JEOL 2010 microscope interfaced with an energy dispersive spectroscopy (EDS). Elemental mapping was analyzed in the STEM mode. XRD patterns were recorded on a Philips PW3040/60 diffractometer with Cu KR (1.5406 Å) radiation.

2.6. Electrochemical Investigation. Electrochemical characterization was studied on a CHI 660C electrochemical analyzer system (Shanghai CHI Instruments Co.) configured to a three-electrode setup under ambient conditions, in which a Pt wire was used as the auxiliary electrode and a saturated calomel electrode (SCE) as the reference electrode. A glassy carbon (GC) disk embedded in Teflon acted as the working electrode, which was polished with 0.5 μm alumina slurry and washed with water and alcohol before use. 4.0 mg of Pt catalysts was dispersed in 400 μL of water to form a catalyst ink with ultrasound. This Pt catalyst ink (2.5 μL) was mixed with an equivolume of 0.5% Nafion117 solution, and then the mixture was dropped and air-dried on the GC electrode at room temperature. Electrochemical tests were measured in a N_2-saturated 0.5 M H_2SO_4 solution with or without 0.5 M CH_3OH.
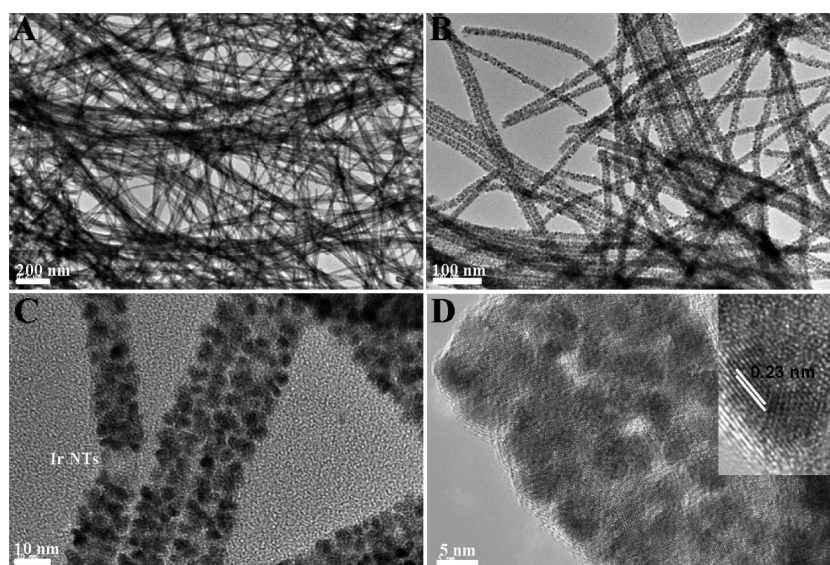
Figure 2. TEM images of PtIrTe NTs under different magnification (A) 200 nm, (B) 100 nm, (C) 10 nm, and (D) 5 nm. Inset: their high resolution TEM image.
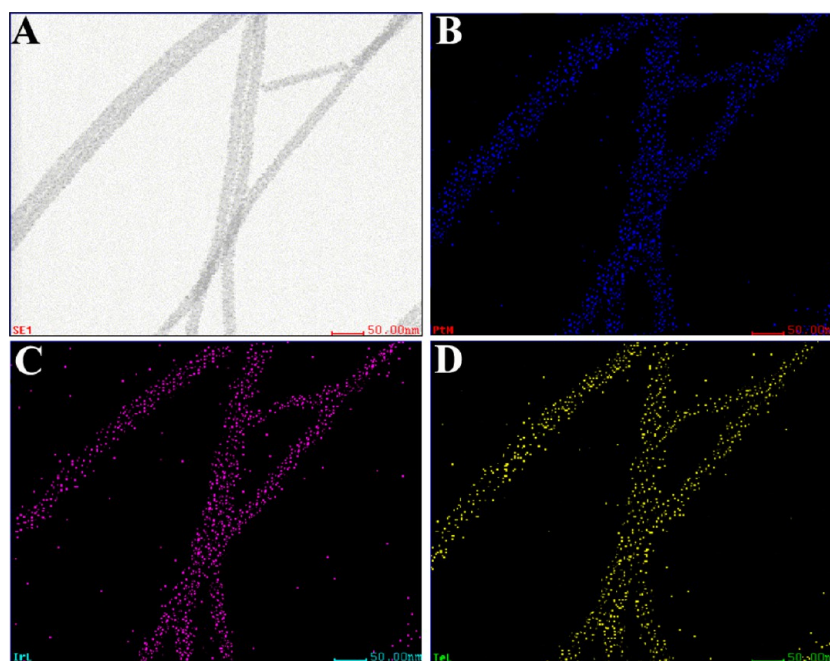

Figure 3. HAADF STEM (A) and elemental mapping of PtIrTe NTs: (B) Pt M, (C) Ir L and (D) Te L.

3. RESULTS AND DISCUSSION

3.1. Materials Characterization. Te nanomaterials are observed by TEM under different magnifications. Figure 1A and B shows that Te NWs reach a length of up to tens of micrometers, and their diameter is averaged to be 7 nm. Their high resolution TEMs (HRTEMs) clearly reveal a 0.592 nm *d*-spacing of adjacent fringes on Te NWs, which can be ascribed to the (001) planes of a hexagonal lattice of Te.[19] IrTe bicomponent hybrids form after Ir takes the place of Te on Te NWs, and these IrTe hybrids are present as nanotubes, which can reach a length of tens of micrometers as Te NWs can (Figure 1C and D). Their external diameter is estimated to be ca. 8 nm and an internal diameter ca. 6 nm. Interestingly, based on the HRTEM, these IrTe NTs are amorphous, different from the specific crystal structure of Te NWs or those of Ir nanoparticles.

After Pt nanoparticles were deposited on the surface of IrTe NTs, as shown in Figure 2A, PtIrTe tricomponent hybrids still maintain a one-dimensional configuration measured up to tens of micrometers almost without shortening. Figure 2A shows the Pt component presented as nanodendrites arrayed on the surface of IrTe NTs. It is difficult to discern IrTe NTs in PtIrTe hybrids due to the high density of Pt nanodendrites deposited on IrTe NTs. However, their fracture plane clearly reveals the presence of IrTe NTs in PtIrTe hybrids, indicative of a core−shell structure of PtIrTe NTs. In this case, IrTe NTs are comprised of the core, while Pt nanodendrites are made up of the shells, which are self-interweaved to create lots of nanopores on IrTe NTs (Figure 2C). The HRTEM exhibits Pt nanodendrites consisting of Pt nanoparticles with a diameter of 3−4 nm, which are aggregated on IrTe NTs. In addition, these Pt nanoparticles also display a
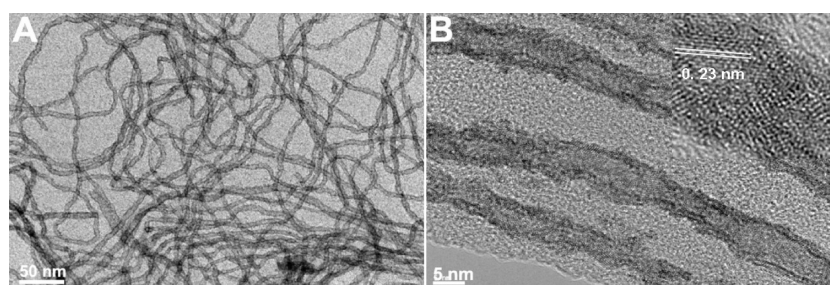
Figure 4. TEM images of PtTe NTs under different magnification (A) 50 nm and (B) 5 nm. Inset: their high resolution TEM image.
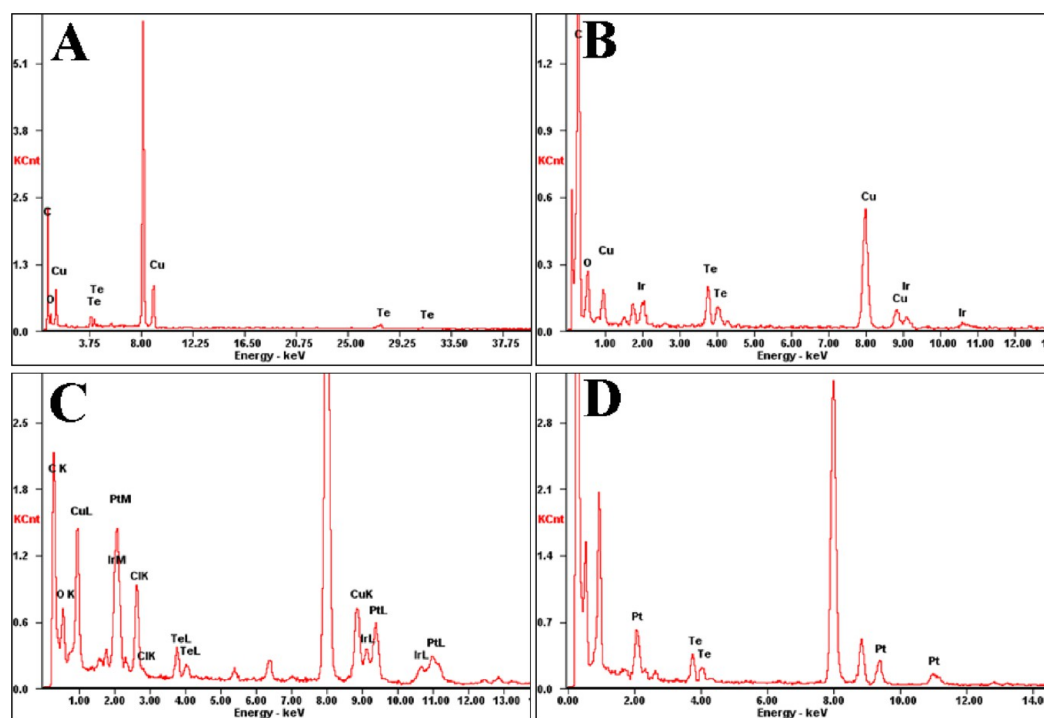

Figure 5. EDS curves of (A) Te NWs, (B) IrTe NTs, (C) PtIrTe NTs, and (D) PtTe NTs.

0.23 nm d-spacing of adjacent fringes assigned to (111) planes of face-centered Pt cubic (fcc)[20] (Figure 2D). The core−shell structure of PtIrTe NTs was further characterized by elemental mapping. Several typical PtIrTe NTs were imaged by the high-angle annular dark-field scanning TEM (HAADF STEM) (Figure 3A), and their element distributions were analyzed by STEM-EDS technique (Figure 3B-D). Observably, Pt, Ir, and Te elements were uniformly distributed among PtIrTe NTs. Moreover, Pt mapping exhibits a higher density of Pt concentration with larger diameter distribution by comparison with those of Ir and Te mapping, which reveals a core−shell nanostructure of the tricomponent hybrids, composed of the IrTe NTs as a core and a complete shell of Pt.

As discussed above, Ir nanoparticles were uniformly dispersed on Te Nanowires to form an amorphous IrTe NTs. These Ir nanoparticles will act as seeds to allow Pt nanoparticles to grow along IrTe. On the other hand, the PVP is also necessary in the formation of PtIrTe NTs. Without PVP, Pt nanoparticles will be dropped off IrTe NTs (Supporting Information, Figure S1).

For comparison, PtTe NTs are also prepared, as shown in Figure 4; PtTe NTs were hollow with a diameter between 5 and 10 nm. HRTEM also reveals a 0.23 nm d-spacing of adjacent fringes, indexed as a (111) plane of fcc Pt cubic crystal.[21]

The composition of Te nanomaterials is determined by the EDS curves attached to TEM. As shown in Figure 5, Te signals are presented at all EDS curves and occur at ca. 3.9 keV (for Te L) and 27.0 keV (for Te K).[22] Both Pt M and Ir M signals are presented at ca. 2.0 keV. Meanwhile, Pt L signals are different from the Ir one. For Pt L signals, they appear at 9.5 keV for Pt La and 11.1 keV for Pt Lb. For Ir L signals, they occur at 9.1 keV for Ir La and 10.6 keV for Ir Lb.[23] By normalizing the L core intensity of Pt, Ir, and Te signals, the molar ratio of Ir, Pt, and Te for different Te nanomaterials is estimated and listed in Table S1. The atomic ratio of Pt, Ir, and Te is estimated to be 5:2:2 for PtIrTe, and these results are in good agreement with those of ICP-AES (Supporting Information, Table S1).

The composition of Te nanomaterials is further confirmed by XPS (Figure 6). All their XPS survey profiles show the C 1s signal at ca. 285 eV and the N 1s signal at ca. 400 eV (Figure 6A), indicating the presence of PVP, which acts as a stabilizer in the formation of Te nanomaterials. Figure 6B exhibits the variation of the Te 3d core level spectra. For Te NWs, Te 3d spectra display two intense peaks ascribed to Te(0) at 573.2 eV for Te (0) 3d 5/2 and 583.5 eV for Te 3d (0) 3/2, respectively. Meanwhile, another couple of weak Te 3d spectra occurs at 577.1 eV for Te (IV) 3d 5/2 and 587.7 eV for Te (IV) 3d 3/2,[24] respectively, which may be associated with the presence of TeO_2
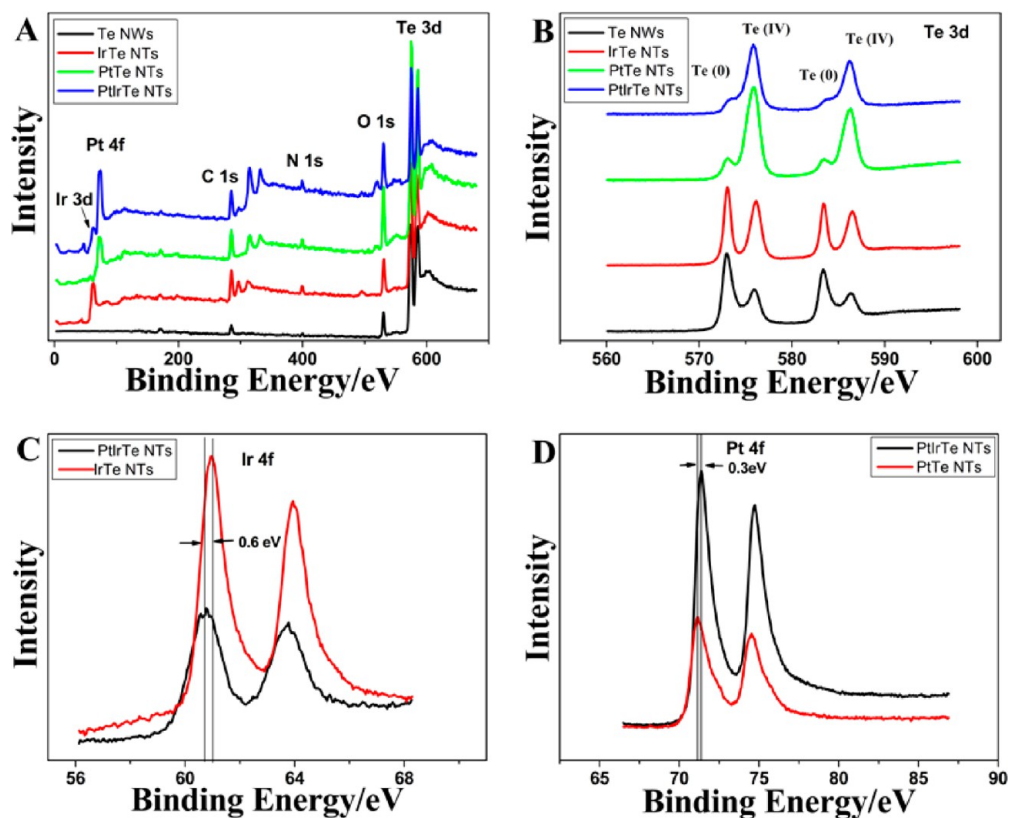
Figure 6. XPS survey spectra (A) of Te NWs, IrTe NTs, PtTe NTs, and PtIrTe NTs and variation in the core level spectra of Te 3d (B), Ir 4f (C), and Pt 4f (D).

generated from the surface oxidation of Te NWs by oxygen in air. Obviously, Pt or Ir introduction decreases significantly the spectra of Te (0) 3d and augments considerably the spectra of Te (IV) 3d, indicating that Te NWs are oxidized and replaced by Pt or Ir elements. Figure 6C presents the Ir 3d core level spectra for IrTe NTs and PtIrTe NTs. For IrTe NTs, the Ir (0) 4f spectra split into 4f 7/2 at 60.8 eV and 4f 5/2 at 63.7 eV.[25] After Pt nanoparticles are deposited onto the IrTe NTs, the Ir (0) 4f 7/2 spectra shift negatively by 0.6 eV. Figure 6D reveals the Pt (0) 4f core level spectra for PtTe NTs and PtIrTe NTs. For PtIrTe NTs, the Pt (0) 4f spectra possess 4f 7/2 at 71.4 eV and 4f 5/2 at 74.7 eV. Their Pt (0) 4f 7/2 signal shifts positively by 0.3 eV in contrast with that of PtTe NTs. This energy shift indicates that the surface Pt shell has received a partial charge from the neighboring Ir component, an evidence for the decrease in the d-band reactivity and the oxygen affinity on Pt surface.[5,23,25,26]

The crystal structure of Te nanomaterials was measured using XRD analysis. As shown in Figure 7, the peak positions of Te NWs are well indexed to the Te hexagonal lattice (JCPDS no. 036-1452).[28] IrTe NTs share the similar XRD pattern with Te NWs, but the peaks intensities of IrTe NTs are much lower than that of Te NWs, demonstrating partial replacement of Te NWs by Ir nanoparticles. However, there are no significant diffraction peaks on the XRD pattern of IrTe NTs, further confirming the amorphous Ir nanoparticles in IrTe NTs. The Te (011) can be observed in the XRD pattern of PtTe NTs and PtIrTe NTs, indicative of the presence of the Te crystal structure in these Pt and Ir hybrids, which may act as a framework for in situ deposition and dispersion of the Pt or the Ir nanoparticle.[5] Besides, Figure 6 shows a well-refined face-centered cubic (fcc) platinum in accordance with the XRD patterns of PtTe NTs and
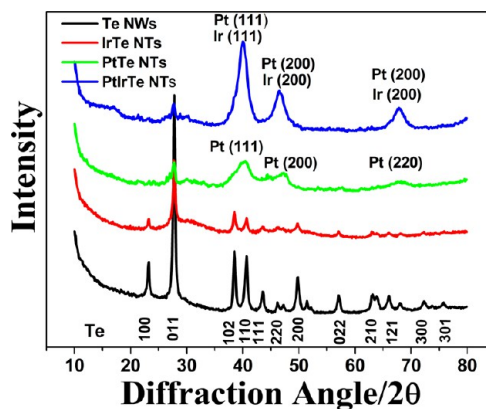

Figure 7. XRD patterns of Te NWs, IrTe NTs, PtTe NTs, and PtIrTe NTs.

PtIrTe NTs; their lattice constant a is calculated to be 3.9 Å according to the Scherrer equation, which fits in with the standard literature values (JCPDS no. 04-0802). In especial, all the diffraction peaks are broadened due to their nanoscale structural features.[15]

3.2. Electrochemical Investigation. The electrochemical behaviors of PtIrTe NTs catalysts were studied by cyclic voltammetry (CV). Figure S2 shows the cyclic voltammograms (CVs) of PtIrTe NTs catalysts in H_2SO_4 (0.5 M) solution for the first and the 40th cycles (Supporting Information). This potential scan could rearrange outer Pt and Ir atoms due to the dissolution of adjacent Te atoms. Pt surfaces are activated because more Pt sites are exposed and available to methanol oxidation.[28−30] The continuous decrease for the peak current of
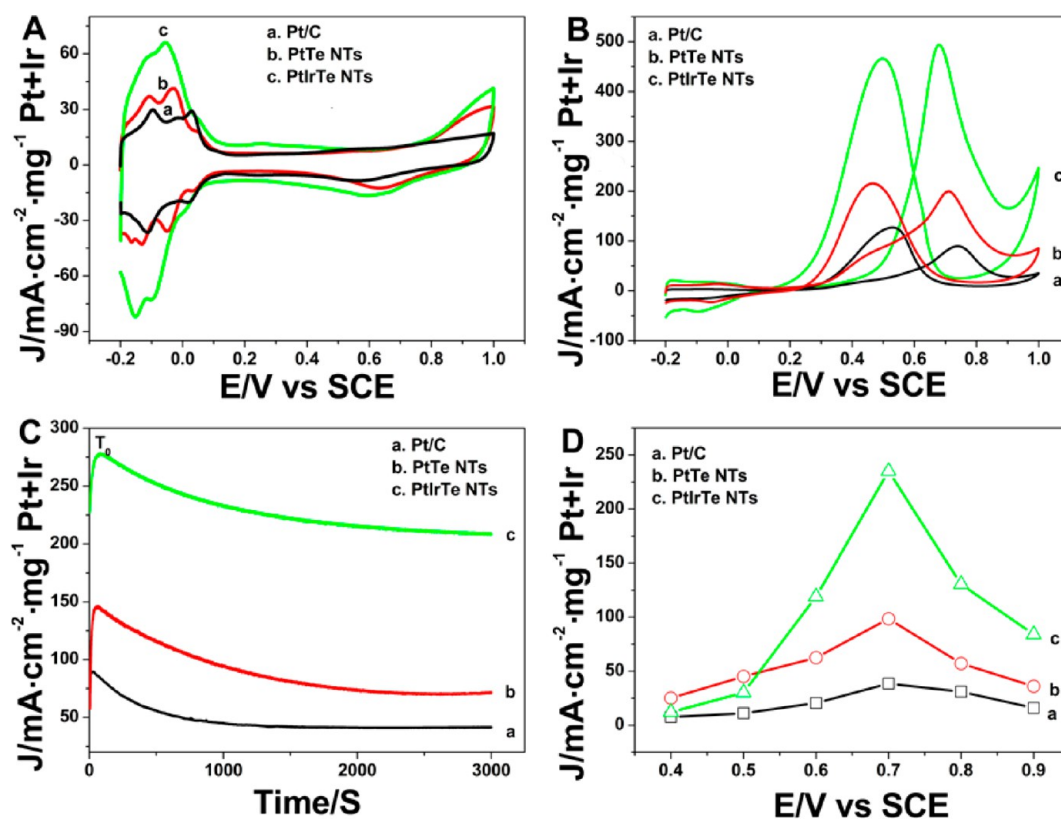
Figure 8. CV curves (A, B) of PtIrTe NTs, PtTe NTs, and Pt/C catalysts in (A) 0.5 M H_2SO_4 and (B) 0.5 M H_2SO_4+0.5 M CH_3OH solution at the scan rate of 50 mV·s^{-1}. Chronoamperometric curves (C) of PtIrTe NTs, PtTe NTs, and Pt/C catalysts for methanol electrooxidation in 0.5 M H_2SO_4+0.5 M CH_3OH solution at the applied potential of 0.60 V. Their potential-dependent steady-state current (D) of methanol electrooxidation for 3000 s polarization.

PtIrTe NTs catalysts between 0.6 and 0.9 V reveals the dissolution of Te atoms in 0.5 M H_2SO_4 solution during the successive potential cycling,[31] thereby enriching Pt and Ir atoms on the surface of PtIrTe NTs catalysts. Meanwhile, the augment in the underpotential deposited hydrogen between −0.2 and 0.15 V indicates the exposure of a PtIr-concentrated skin.[5] As shown in Figure 8A, this CV loop in the hydrogen region can be used to measure the electrochemically active surface area (ECSA) of Pt based catalysts by integrating the hydrogen region area after deducting the double-layer capacitor.[32] Based on the normalization to the real surface area per mass of Pt and Ir elments, the PtIrTe TNs catalysts have an ECSA of 108 mA·cm^{-2}·mg^{-1}, almost twice as much as PtTe TNs catalysts (58 mA·cm^{-2}·mg^{-1}). In contrast, the ECSA of Pt/C catalysts is also determined, which is 49 mA·cm^{-2}·mg^{-1}, close to that of PtTe TNs catalysts. The high ECSA of PtIrTe TNs catalysts may result from their nanoporous core−shell structure.

The MOR was tested at the GC electrodes modified with Pt catalysts in 0.5 M H_2SO_4 solution containing 0.5 M methanol. Figure 8B shows a well-known dependence of the faradic current response on the applied potential for the methanol electrooxidation. The forward peak $I_{methanol}$ at ca. 0.7 V is assigned to the oxidation of methanol. The reverse peak I_{co} at ca. 0.5 V is ascribed to the oxidation of intermediate, dominated by adsorbed CO.[33] Clearly, $I_{methanol}$ of PtIrTe NTs catalysts (495 mA·cm^{-2}·mg^{-1}) is almost 2.5 times higher than that of PtTe NTs (200 mA·cm^{-2}·mg^{-1}) and 5 times that of Pt/C catalysts (90 mA·cm^{-2}·mg^{-1}). In contrast, IrTe NTs show no significant response to the oxidation of methanol oxidation (Supporting Information, Figure S3). The high catalytic efficiency of methanol is attributed to the large

ECSA value from their 1D nanoporous structure. Moreover, these results are comparable or superior to those of the current state-of-art Pt catalysts, such as PtPdTe NWs (595 mA·cm^{-2}·mg^{-1})[5] and PtRu/Graphite Carbon Nanofibers composite (∼240 mA·cm^{-2}·mg^{-1}).[33] In addition, a large ratio of $I_{methanol}$/I_{co} suggests a more complete methanol oxidation, a lower concentration of intermediate species adsorbed on the active site of Pt plane, and thus a higher resistance to CO poisoning.[33−35] The $I_{methanol}$/I_{co} of PtIrTe NTs catalysts is 1.10, higher than 0.99 of PtTe NTs catalysts and 0.68 of Pt/C catalysts, suggesting a higher CO tolerance of PtIrTe NTs catalysts by comparison with PtTe NTs and Pt/C catalysts. The introduction of Ir to Pt catalysts may accord for the enhanced resistance of PtIrTe NTs catalysts to CO poisoning, as a result of the modification to the electronic structure of the Pt site by the neighboring Ir atom. This variation on the Pt electronic structure can lower the adsorptive capability of the Pt site to the intermediate species and accelerate C−H cleavage on the Pt plane due to the electron shift of Pt sites to the d-band center of Ir atoms.[36,37] Thus, the PtIrTe NTs can clear the CO byproducts away more quickly than PtTe NTs or Pt/C catalysts.[5]

Figure 8C shows the representative amperometric currents recorded at 0.6 V in 0.5 M H_2SO_4 solution containing 0.5 M methanol. The MOR currents decay for all Pt catalysts at the start. This decrease is associated with the deactivation of the Pt sites by the intermediate from MOR. Then the MOR currents will remain stable after the intermediate species on the Pt surface achieve the equilibrium of adsorption/desorption.[33] The long-term poisoning rate (δ) can be used to evaluate the stability of Pt

21991

dx.doi.org/10.1021/am5047747 | ACS Appl. Mater. Interfaces 2014, 6, 21986−21994

catalysts. It is estimated according to the linear current decay of MOR using the following equation[5,38]

$$\delta(\% \ s^{-1}) = \frac{100}{I_0} \times \left(\frac{dI}{dt}\right)_{t > 500s}$$

where $(dI/dt)_{t>500s}$ is the slope of the linear portion on the current decay, and I_0 is the current at the start of polarization back extrapolated from the linear current decay.

The long-term poisoning rate of PtIrTe NTs catalysts is 0.012 s^{-1}, close to 0.015 s^{-1} of PtTe NTs catalysts and less than 0.024 s^{-1} of Pt/C catalysts. These results confirm the superior stability of PtIrTe NTs catalysts over PtTe NTs and Pt/C catalysts.

In addition, PtIrTe NTs catalysts show a higher current response (209 mA·cm^{-2}·mg^{-1}) than PtTe NTs (71 mA·cm^{-2}·mg^{-1}) or Pt/C (40 mA·cm^{-2}·mg^{-1}) catalysts under over 3000 s^{-1} continuous polarizing at 0.6 V. Moreover, Figure 8D indicates that the PtIrTe NTs catalysts exhibit better performance on MOR than Pt/C catalysts for all applied potentials.

The poison tolerance of Pt catalysts was further investigated by CO stripping voltammetry; the CO was polarized and adsorbed at Pt catalysts at −0.10 V in a CO-saturated 0.5 M H$_2$SO$_4$ for 15 min. Then the CO in solution was removed by purging N$_2$ for 15 min. Figure 9 shows only a well-defined CO$_{ad}$ oxidative wave
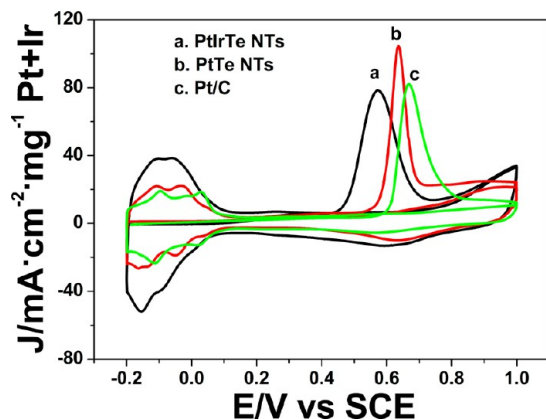

Figure 9. CO stripping CV curves of the different Pt-based catalysts in 0.5 M H$_2$SO$_4$ solution at the scan rate of 50 mV·s^{-1}.

recorded on the CVs of PtIrTe NTs and PtTe NTs catalysts, indicating a synergistic effect[39] on the CO$_{ad}$ oxidation from a combinative contribution of Pt and Ir sites. The oxidation of

CO$_{ad}$ starts at 0.432 V and reaches its peak at 0.571 V for PtIrTe NTs catalysts, shifting negatively by 0.093 and 0.066 V as compared to those on PtTe NTs catalysts. The results demonstrate that PtIrTe NTs catalysts are more active for CO$_{ad}$ than PtTe NTs catalysts. Obviously, Ir plays a positive role in CO tolerance for Pt catalysts, in accordance with a previous report on the PtIr-IrO$_2$ NT thin-wall electrode at this point.[40] On the other hand, PtIrTe NTs catalysts also show a negative shift (0.099 V) of peak potential from CO$_{ad}$ oxidation by comparison with the Pt/C catalyst. The result suggests a faster oxidative removal of CO$_{ad}$ that takes place at PtIrTe NTs. As discussed above, the electronic structure of Pt surface was modified after the Ir addition. This modification can strengthen the repulsive interaction between CO$_{ad}$ and quicken the oxidative removal of CO$_{ad}$.[26]

The structural stability of PtIrTe NTs and PtTe NTs catalysts was valued by cyclic voltammetry and TEM. These Pt catalysts were swept between −0.2 and 1.0 V in 0.5 M H$_2$SO$_4$ solution for 5000 cycles at room temperature. Then the samples were peeled off and dispersed into an alcohol solution with ultrasound. The CV curves of the PtIrTe NTs and PtTe NTs catalysts before and after 5000 CV cycles are shown in Figure 10A. The peak current in the hydrogen region for the PtTe NTs catalysts drops remarkably during the successive potential circling. On the contrary, the PtIrTe NTs catalysts display only a slight decay in the peaks current under the same condition. Figure 10B shows the ECSA retention with the cycle number of CV tests. After 5000 cycles, the ECSA of the PtIrTe NTs catalysts only decreased by 15%, while PtTe NTs catalysts lost 40% of their ECSAs. TEM images show that most of the PtIrTe NTs were broken after 5000 CV cycles, and the small Pt nanodendrites were agglomerated into larger particles (Supporting Information, Figure S4A and B). Similarly, PtTe NTs were also cracked, and some large Pt nanoparticles can be observed (Supporting Information, Figure S4C and D). The morphological variation of PtTe NTs and PtTe NTs can be ascribed to a combination of the dissolution of Te framework and the Ostwald ripening of Pt nanoparticles.[41]

4. CONCLUSIONS

We have developed a template approach to mass production of porous, uniform, and ultralong PtIrTe NTs, which exhibits a larger ECSA value, a higher CO tolerance, and a larger electrocatalytic activity toward methanol oxidation reaction (MOR) by comparison with Pt/C due to a combination of the
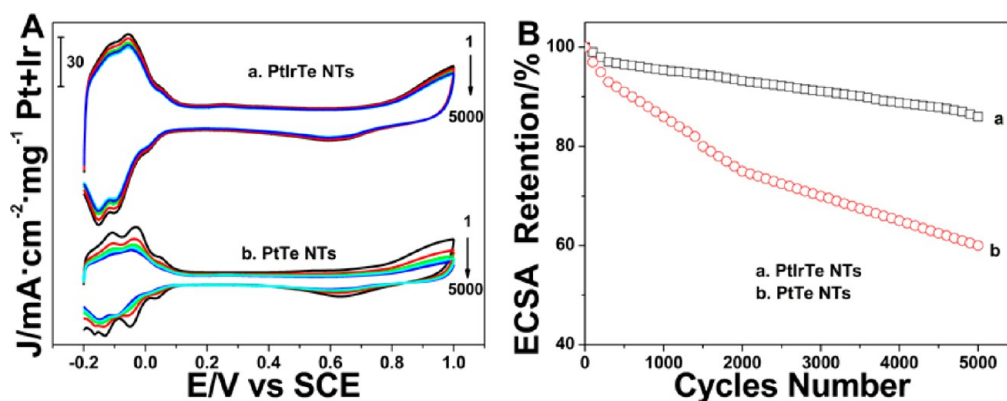

Figure 10. Electrochemical stability of PtIrTe NTs and PtTe NTs catalysts as shown in the CV curves before and after the durability tests in 0.5 M H$_2$SO$_4$ solutions at the scan rate of 50 mV·s^{-1}. The ECSA retention of PtIrTe NTs and PtTe NTs catalysts with CV cycles number.

nanoporous core—shell structure and the beneficial electron structure after the introduction of Ir into the Pt site. These PtIrTe NTs exhibit a current response to methanol oxidation up to 495 mA·cm^{-2}·mg^{-1}, which is comparable or superior to those so far reported for the Pt based catalysts. The PtIrTe NTs catalysts can maintain a MOR current of 209 mA·cm^{-2}·mg^{-1} for 3000 s polarization at 0.6 V with a long-term poisoning rate of 0.012 s^{-1}. Therefore, these superior properties of PtIrTe NTs catalysts hold promising use as an alternative anode material for DMFCs on an increasingly large scale.

■ ASSOCIATED CONTENT

Ⓢ Supporting Information

Table of Composition data for Te hybrids, TEM images of PtIrTe NTs prepared without PVP, TEM images of PtIrTe NTs and PtTe NTs after 5000 CV circling, the successive 40th CV curves of PtIrTe NTs and CV curves of IrTe NTs. This material is available free of charge via the Internet at http://pubs.acs.org.

■ AUTHOR INFORMATION

Corresponding Author
*Phone/Fax: +86 579 82282269. E-mail: jhyuan@zjnu.cn.
Notes
The authors declare no competing financial interest.

■ ACKNOWLEDGMENTS

■ REFERENCES

(1) Zhang, H.; Jin, M.; Xia, Y. Enhancing the Catalytic and Electrocatalytic properties of Pt-based Catalysts by Forming Bimetallic Nanocrystals with Pd. *Chem. Soc. Rev.* **2012**, *41*, 8035–8049.

(2) Huang, H.; Sun, D.; Wang, X. Low-Defect MWNT-Pt Nanocomposite as a High Performance Electrocatalyst for Direct Methanol Fuel Cells. *J. Phys. Chem. C* **2011**, *115*, 19405–19412.

(3) Kua, J.; Goddard, W. A. Oxidation of Methanol on 2nd and 3rd Row Group VIII Transition Metals (Pt, Ir, Os, Pd, Rh, and Ru): Application to Direct Methanol Fuel Cells. *J. Am. Chem. Soc.* **1999**, *121*, 10928–10941.

(4) Zhang, C.; Hwang, S. Y.; Trout, A.; Peng, Z. Solid-state Chemistry-enabled Scalable Production of Octahedral Pt-Ni Alloy Electrocatalyst for Oxygen Reduction Reaction. *J. Am. Chem. Soc.* **2014**, *136*, 7805–7808.

(5) Li, H. H.; Zhao, S.; Gong, M.; Cui, C. H.; He, D.; Liang, H. W.; Wu, L.; Yu, S. H. Ultrathin PtPdTe Nanowires as Superior Catalysts for Methanol Electrooxidation. *Angew. Chem., Int. Ed. Engl.* **2013**, *125*, 7620–7624.

(6) Gu, J.; Zhang, Y. W.; Tao, F. F. Shape Control of Bimetallic Nanocatalysts through Well-designed Colloidal Chemistry Approaches. *Chem. Soc. Rev.* **2012**, *41*, 8050–8065.

(7) Yang, H. Platinum-based Electrocatalysts with Core-shell Nanostructures. *Angew. Chem., Int. Ed. Engl.* **2011**, *50*, 2674–2676.

(8) Wang, D.; Li, Y. Bimetallic Nanocrystals: Liquid-phase Synthesis and Catalytic Applications. *Adv. Mater.* **2011**, *23*, 1044–1060.

(9) Guo, S.; Dong, S.; Wang, E. Ultralong Pt-on-Pd Bimetallic Nanowires with Nanoporous Surface: Nanodendritic Structure for Enhanced Electrocatalytic Activity. *Chem. Commun.* **2010**, *46*, 1869–1871.

(10) Xia, B. Y.; Wu, H. B.; Yan, Y.; Lou, X. W.; Wang, X. Ultrathin and Ultralong Single-crystal Platinum Nanowire Assemblies with Highly Stable Electrocatalytic Activity. *J. Am. Chem. Soc.* **2013**, *135*, 9480–9485.

(11) Chen, J.; Herricks, T.; Xia, Y. Polyol Synthesis of Platinum Nanostructures: Control of Morphology through the Manipulation of Reduction Kinetics. *Angew. Chem., Int. Ed. Engl.* **2005**, *117*, 2645–2648.

(12) Wang, D.; Luo, H.; Kou, R.; Gil, M. P.; Xiao, S.; Golub, V. O.; Yang, Z.; Brinker, C. J.; Lu, Y. A General Route to Macroscopic Hierarchical 3D Nanowire Networks. *Angew. Chem., Int. Ed. Engl.* **2004**, *116*, 6295–6299.

(13) Yuan, J.; Wang, K.; Xia, X. Highly Ordered Platinum-Nanotubule Arrays for Amperometric Glucose Sensing. *Adv. Funct. Mater.* **2005**, *15*, 803–809.

(14) Alia, S. M.; Zhang, G.; Kisailus, D.; Li, D.; Gu, S.; Jensen, K.; Yan, Y. Porous Platinum Nanotubes for Oxygen Reduction and Methanol Oxidation Reactions. *Adv. Funct. Mater.* **2010**, *20*, 3742–3746.

(15) Liang, H. W.; Liu, S.; Gong, J. Y.; Wang, S. B.; Wang, L.; Yu, S. H. Ultrathin Te Nanowires: An Excellent Platform for Controlled Synthesis of Ultrathin Platinum and Palladium Nanowires/Nanotubes with very High aspect Ratio. *Adv. Mater.* **2009**, *21*, 1850–1854.

(16) Sakamoto, Y.; Fukuoka, A.; Higuchi, T.; Shimomura, N.; Inagaki, S.; Ichikawa, M. Synthesis of Platinum Nanowires in Organic-inorganic Mesoporous Silica Templates by Photoreduction: Formation Mechanism and Isolation. *J. Phys. Chem. B* **2004**, *108*, 853–858.

(17) Liu, L.; Pippel, E. Low-Platinum-Content Quaternary PtCuCoNi Nanotubes with Markedly Enhanced Oxygen Reduction Activity. *Angew. Chem., Int. Ed. Engl.* **2011**, *50*, 2729–2733.

(18) Mayers, B.; Jiang, X.; Sunderland, D.; Cattle, B.; Xia, Y. Hollow Nanostructures of Platinum with Controllable Dimensions Can Be Synthesized by Templating against Selenium Nanowires and Colloids. *J. Am. Chem. Soc.* **2003**, *125*, 13364–13365.

(19) She, G.; Shi, W.; Zhang, X.; Wong, T.; Cai, Y.; Wang, N. Template-free Electrodeposition of One-dimensional Nanostructures of Tellurium. *Cryst. Growth Des.* **2008**, *9*, 663–666.

(20) Li, M.; Cullen, D. A.; Sasaki, K.; Marinkovic, N. S.; More, K.; Adzic, R. R. Ternary Electrocatalysts for Oxidizing Ethanol to Carbon Dioxide: Making Ir Capable of Splitting C-C Bond. *J. Am. Chem. Soc.* **2012**, *135*, 132–141.

(21) Chen, X.; Zang, W.; Vimalanathan, K.; Iyer, K. S.; Raston, C. L. A Versatile Approach for Decorating 2D Nanomaterials with Pd or Pt Nanoparticles. *Chem. Commun.* **2013**, *49*, 1160–1162.

(22) Liu, J.-W.; Zhu, J.-H.; Zhang, C.-L.; Liang, H.-W.; Yu, S.-H. Mesostructured Assemblies of Ultrathin Superlong Tellurium Nanowires and Their Photoconductivity. *J. Am. Chem. Soc.* **2010**, *132*, 8945–8952.

(23) Lee, K.-S.; Cho, Y.-H.; Jeon, T.-Y.; Yoo, S. J.; Park, H.-Y.; Jang, J. H.; Sung, Y.-E. Surface Structures and Electrochemical Activities of PtRu Overlayers on Ir Nanoparticles. *ACS Catal.* **2012**, *2*, 739–745.

(24) Samal, A.; Pradeep, T. Pt$_3$Te$_4$ Nanoparticles from Tellurium Nanowires. *Langmuir* **2010**, *26*, 19136–19141.

(25) El Sawy, E. N.; Birss, V. Electrodeposited Pt-Ir Thin Films as DMFC Anode Materials. *ECS Trans.* **2010**, *28*, 195–201.

(26) Nilekar, A. U.; Sasaki, K.; Farberow, C. A.; Adzic, R. R.; Mavrikakis, M. Mixed-metal Pt Monolayer Electrocatalysts with Improved CO Tolerance. *J. Am. Chem. Soc.* **2011**, *133*, 18574–18576.

(27) Safdar, M.; Wang, Z.; Mirza, M.; Butt, F. K.; Wang, Y.; Sun, L.; He, J. Telluride-based Nanorods and Nanosheets: Synthesis, Evolution and Properties. *J. Mater. Chem. A* **2013**, *1*, 1427–1432.

(28) Li, H. H.; Cui, C. H.; Zhao, S.; Yao, H. B.; Gao, M. R.; Fan, F. J.; Yu, S. H. Mixed-PtPd-Shell PtPdCu Nanoparticle Nanotubes Templated from Copper Nanowires as Efficient and Highly Durable Electrocatalysts. *Adv. Energy Mater.* **2012**, *2*, 1182–1187.

(29) Oezaslan, M.; Heggen, M.; Strasser, P. Size-dependent Morphology of Dealloyed Bimetallic Catalysts: Linking the Nano to the Macro scale. *J. Am. Chem. Soc.* **2011**, *134*, 514–524.

(30) Cui, C. H.; Liu, X. J.; Li, H. H.; Gao, M. R.; Liang, H. W.; Yao, H. B.; Yu, S. H. Ternary PtPdCu Electrocatalyst Formed through Surface: Atomic Redistribution against Leaching. *ChemCatChem* **2012**, *4*, 1560–1563.

(31) Li, X.; Liu, L.; Lee, J.-W.; Popov, B. N. Development of Tellurium-modified Carbon Catalysts for Oxygen Reduction Reaction in PEM Fuel Cells. *J. Power Sources* **2008**, *182*, 18−23.

(32) Wu, B.; Hu, D.; Kuang, Y.; Liu, B.; Zhang, X.; Chen, J. Functionalization of Carbon Nanotubes by an Ionic-Liquid Polymer: Dispersion of Pt and PtRu Nanoparticles on Carbon Nanotubes and Their Electrocatalytic Oxidation of Methanol. *Angew. Chem., Int. Ed. Engl.* **2009**, *48*, 4751−4754.

(33) Hsin, Y. L.; Hwang, K. C.; Yeh, C.-T. Poly(vinylpyrrolidone)-modified Graphite Carbon Nanofibers as Promising Supports for PtRu Catalysts in Direct Methanol Fuel Cells. *J. Am. Chem. Soc.* **2007**, *129*, 9999−10010.

(34) Deivaraj, T.; Lee, J. Y. Preparation of Carbon-supported PtRu Nanoparticles for Direct Methanol Fuel Cell Applications: A Comparative Study. *J. Power Sources* **2005**, *142*, 43−49.

(35) Gu, Y.-J.; Wong, W.-T. Nanostructure PtRu/MWNTs as Anode Catalysts Prepared in a Vacuum for Direct Methanol Oxidation. *Langmuir* **2006**, *22*, 11447−11452.

(36) Wang, D.-Y.; Chou, H.-L.; Lin, Y.-C.; Lai, F.-J.; Chen, C.-H.; Lee, J.-F.; Hwang, B.-J.; Chen, C.-C. Simple Replacement Reaction for the Preparation of Ternary $Fe_{1-x}PtRu_x$ Nanocrystals with Superior Catalytic Activity in Methanol Oxidation Reaction. *J. Am. Chem. Soc.* **2012**, *134*, 10011−10020.

(37) Ferrin, P.; Mavrikakis, M. Structure Sensitivity of Methanol Electrooxidation on Transition Metals. *J. Am. Chem. Soc.* **2009**, *131*, 14381−14389.

(38) Guo, J.; Zhao, T.; Prabhuram, J.; Chen, R.; Wong, C. Preparation and Characterization of A PtRu/C Nanocatalyst for Direct Methanol Fuel Cells. *Electrochim. Acta* **2005**, *51*, 754−763.

(39) Freitas, R. G.; Pereira, E. P.; Antunes, E. C. CO and Methanol Electrooxidation on Pt/Ir/Pt Multilayers Electrodes. *Electrochim. Acta* **2009**, *54*, 1999−2003.

(40) Shan, C.-C.; Tsai, D.-S.; Huang, Y.-S.; Jian, S.-H.; Cheng, C.-L. Pt-Ir-IrO_2NT Thin-Wall Electrocatalysts Derived from IrO_2 Nanotubes and Their Catalytic Activities in Methanol Oxidation. *Chem. Mater.* **2007**, *19*, 424−431.

(41) Mayrhofer, K. J. J.; Meier, J. C.; Ashton, S. J.; Wiberg, G. K. H.; Kraus, F.; Hanzlik, M.; Arenz, M. Fuel Cell Catalyst Degradation on the Nanoscale. *Electrochem. Commun.* **2008**, *10*, 1144−1147.